

# Isovalent alloying assisted anomalous valley Hall effect in hexagonal antiferromagnetic monolayer

San-Dong Guo<sup>1</sup>, Liguo Zhang<sup>1</sup>, Xiao-Shu Guo<sup>1</sup> and Gangqiang Zhu<sup>2</sup>

<sup>1</sup>*School of Electronic Engineering, Xi'an University of Posts and Telecommunications, Xi'an 710121, China and*

<sup>2</sup>*School of Physics and Electronic Information, Shaanxi Normal University, Xi'an 716000, Shaanxi, China*

Exploring combination of antiferromagnetic (AFM) spintronics and anomalous valley Hall effect (AVHE) is one of the most important questions for valleytronic applications. The key to address this issue is to achieve spin splitting around the valleys in AFM systems. Here, we propose a possible way for achieving AVHE in hexagonal AFM monolayer, which involves the isovalent alloying. This can break the combined symmetry ( $PT$  symmetry) of spatial inversion ( $P$ ) and time reversal ( $T$ ), giving rise to spin splitting. More specifically, the large spin splitting around the Fermi energy level owes to  $d$  orbital mismatch among these different transition metal ions. Based on first-principles calculations, the proposed way can be verified in out-of-plane AFM  $\text{CrMoC}_2\text{S}_6$  monolayer, which possesses spontaneous valley polarization and spitting splitting, providing possibility to realize AVHE. It is also proved that tensile strain can strengthen the valley splitting and maintain the out-of-plane AFM ordering. Our works provide an experimentally feasible way for developing AFM valleytronic devices.

Keywords: Valley, Antiferromagnetism, Isovalent alloying

Email:sandongyuwang@163.com

## I. INTRODUCTION

Valleys, as an additional degree of freedom of electrons besides charge and spin, lay the foundation for applications in information encoding and processing[1–4]. The discovery and successful preparation of rich two-dimensional (2D) materials promote the development of valley concept due to the large separation in momentum space. 2D transition metal dichalcogenides (TMDs) possess intrinsic broken inversion symmetry and large spin-orbital coupling (SOC), and they are widely recognized as the most representative valleytronic materials with a pair of degenerate but inequivalent -K and K valleys in the reciprocal space[5–10]. However, spontaneous valley polarization lacks in these nonmagnetic TMD monolayers, and some external methods can achieve valley polarization, such as external magnetic field, proximity effect, magnetic doping and light excitation[9–12]. Although these methods can achieve valley polarization, they have many shortcomings, such as small valley splitting, destruction of crystal structure and limited carrier life.

Compared with external methods, the intrinsic valley polarization is highly desirable. Fortunately, the ferrovalley semiconductor has been proposed[13], which possesses intrinsic valley polarization and can achieve anomalous valley Hall effect (AVHE). The ferrovalley materials are generally built on ferromagnetic (FM) hexagonal symmetric systems with broken spatial inversion symmetry[13–22]. Compared to FM materials, antiferromagnetic (AFM) materials possess the high storage density, robustness against external magnetic field, as well as the ultrafast writing speed[23]. Therefore, realizing valley polarization and AVHE in AFM materials is more meaningful for valleytronic application. However, 2D AFM valleytronic materials with intrinsic valley polarization and realizable AVHE are still scarce. Only a few candidate systems have been pro-

posed, such as  $\text{MnPSe}_3/\text{Sc}_2\text{CO}_2$  or  $\text{Cr}_2\text{CH}_2/\text{Sc}_2\text{CO}_2$  heterojunction[24, 25] and Janus  $\text{Mn}_2\text{P}_2\text{X}_3\text{Y}_3$  ( $X, Y=\text{S, Se Te; } X\neq Y$ ) monolayers[26].

In particular, the presence of spin degeneracy poses a significant obstacle to realize AVHE in AFM systems. The out-of-plane external electric field has been used to induce spin splitting in AFM systems, such as A-type AFM hexagonal monolayer  $\text{Cr}_2\text{CH}_2$  and tetragonal monolayer  $\text{Fe}_2\text{BrMgP}$ [27, 28]. This can be explained by the introduction of layer-dependent electrostatic potential caused by out-of-plane external electric field, and the spin order of spin splitting can be reversed by flipping the direction of electric field. In fact, the AVHE can be achieved in electric-potential-difference antiferromagnetism (EPD-AFM) without external electric field[27, 28], which can be equivalently replaced by a built-in electric field caused by Janus structure.

Here, we propose a way to achieve spin splitting by isovalent alloying, and then realize AVHE in hexagonal AFM monolayer. The proposed way can produce large spin splitting around the Fermi energy level, which is due to  $d$  orbital mismatch among these magnetic atoms. By first-principles calculations, we translate our proposed way into  $\text{CrMoC}_2\text{S}_6$  monolayer and clarify the isovalent alloying assisted AVHE in hexagonal AFM monolayer.

## II. WAYS TO ACHIEVE AVHE

The isovalent alloying assisted AVHE in hexagonal AFM monolayer is schematically illustrated in **Figure 1**. **Figure 1** (a) shows that the two magnetic atoms of a hexagonal AFM monolayer per unit cell are the same  $3d$  elements, and its energy extrema of conduction/valance bands is at high symmetry -K/K point. We assume that the lattice of hexagonal AFM monolayer has spatial inversion symmetry, but the AFM ordering leads to the

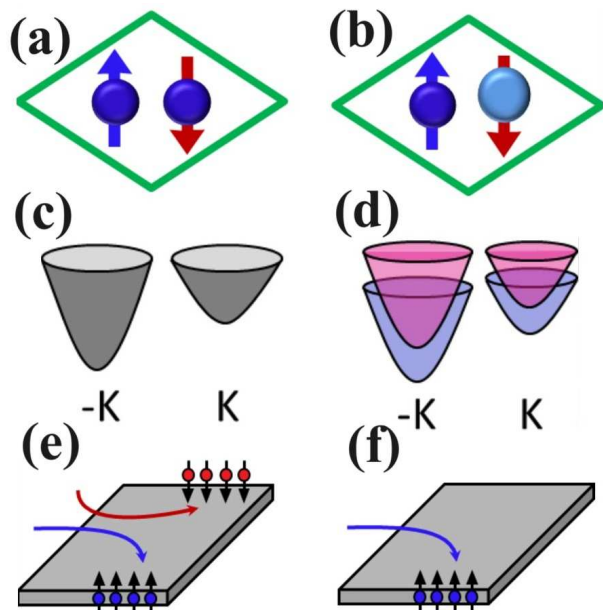


FIG. 1. (Color online) (a) and (c): a hexagonal  $3d$ -AFM monolayer with spin degeneracy but nonequivalent  $-K$  and  $K$  valleys; (b) and (d): via isovalent alloying, (a) becomes  $3d$ - and  $4d$ -AFM monolayer with removed spin degeneracy, and the  $-K$  and  $K$  valleys still are unequal; In the presence of a longitudinal in-plane electric field, an appropriate electron doping for two cases produces valley-spin hall effect (e) and AVHE (f).

simultaneously broken inversion ( $P$ ) symmetry and time reversal ( $T$ ) symmetry, which produces spontaneous valley polarization (Figure 1 (c)). However, the system possesses  $PT$  symmetry, which gives rise to spin degeneracy, prohibiting the realization of AVHE. Due to  $PT$  symmetry, the zero berry curvature ( $\Omega(k)$ ) everywhere in the momentum space can be observed. However, the Berry curvatures for the spin-up and spin-down channels are nonzero, and they are equal in magnitude and opposite in sign. In the presence of a longitudinal in-plane electric field, an appropriate electron doping produces valley-spin Hall effect (Figure 1 (e)).

Here, substituting elements via isovalent alloying (One of the two magnetic atoms is replaced by a  $4d$  element with the same outer electrons.) can be applied to break the  $PT$  symmetry (Figure 1 (b)), and the spin degeneracy of  $-K$  and  $K$  valleys can be removed. Our proposed system can be called asymmetric AFM semiconductor (AAFMS) [29]. Although the two magnetic atoms ( $3d$  and  $4d$  elements) have the same surrounding atomic arrangement, the energy level of  $4d$  electron is higher than that of  $3d$  one ( $d$  orbital mismatch), producing spin splitting. Due to broken  $PT$  symmetry, the spin splitting of the  $-K$  and  $K$  valleys can be observed (Figure 1 (d)), resulting in the AVHE (Figure 1 (f)).

For bulk materials, the AAFMS has been predicted in a family of double perovskites  $A_2CrMO_6$  ( $A = Ca, Sr, Ba$ , and  $M = Ru, Os$ ) [29]. The large spin polarization around

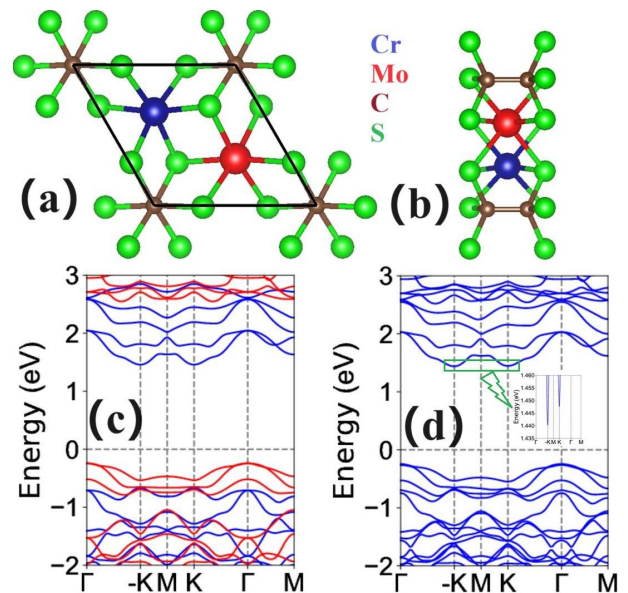


FIG. 2. (Color online) For monolayer  $CrMoC_2S_6$ , (a) and (b): the top and side views of crystal structures; (c) and (d): the energy band structures without SOC and with SOC. In (c), the spin-up and spin-down channels are depicted in blue and red. In (d), the inset shows the enlarged portion of conduction bands near the Fermi energy level.

the Fermi energy level has been observed due to  $d$  orbital mismatch among these magnetic ions. For 2D materials,  $CrMoA_2S_6$  ( $A = C, Si, \text{ or } Ge$ ) monolayers are AAFMSs,  $CrMoC_2S_6$  of which has the highest Néel temperature of 556 K with robust magnetism against carrier doping and external in-plane strain [30]. Next, we take  $CrMoC_2S_6$  monolayer as an example to illustrate our proposal.

### III. COMPUTATIONAL DETAIL

We perform the spin-polarized first-principles calculations within density functional theory (DFT) [31] by using the projector augmented-wave (PAW) method, as implemented in Vienna ab initio Simulation Package (VASP) [32–34]. We use the generalized gradient approximation of Perdew-Burke-Ernzerhof (PBE-GGA) [35] as the exchange-correlation functional. The kinetic energy cutoff of 500 eV, total energy convergence criterion of  $10^{-8}$  eV, and force convergence criterion of  $0.0001 \text{ eV} \cdot \text{\AA}^{-1}$  are set to obtain the accurate results. To describe the strong correlation interaction of  $3d$  and  $4d$  electrons in  $CrMoC_2S_6$ , a Hubbard correction  $U_{eff} = 3.0 \text{ eV}$  [30] is used by the rotationally invariant approach proposed by Dudarev et al [36]. The SOC is incorporated for investigation of valley splitting and magnetic anisotropy energy (MAE). To avoid the interaction between adjacent layers, the vacuum space of more than  $20 \text{ \AA}$  along  $z$  direction is adopted. A  $12 \times 12 \times 1$   $\Gamma$ -centered Monkhorst-Pack grid is used to sample the Brillouin zone (BZ). Based on finite

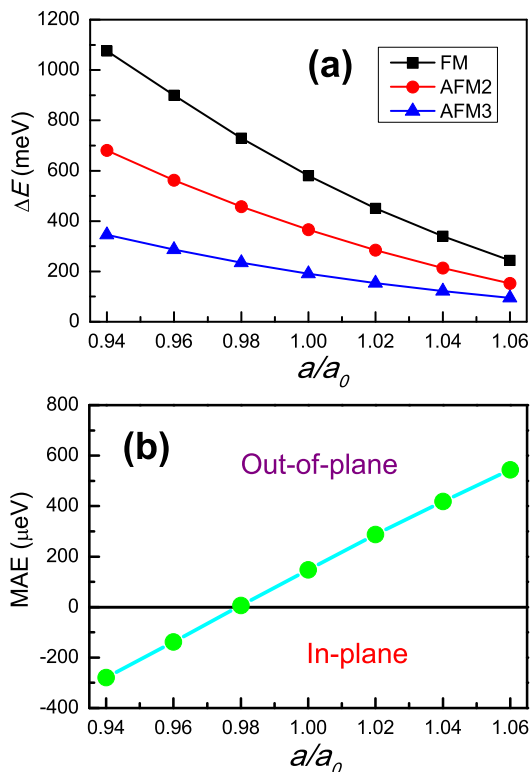


FIG. 3. (Color online) For  $\text{CrMoC}_2\text{S}_6$ , (a): the energy difference between FM/AFM2/AFM3 and AFM1 orderings as a function of  $a/a_0$ ; (b): the MAE vs  $a/a_0$ .

displacement method, the interatomic force constants (IFCs) are calculated by employing  $3 \times 3 \times 1$  supercell, and the phonon dispersion spectrum is obtained by the Phonopy code[37]. The elastic stiffness tensor  $C_{ij}$  are calculated by using strain-stress relationship (SSR) method. The  $C_{ij}^{2D}$  has been renormalized by  $C_{ij}^{2D} = L_z C_{ij}^{3D}$ , where the  $L_z$  is the length of unit cell along  $z$  direction. The Berry curvatures are calculated directly from the calculated wave functions based on Fukui's method[38], as implemented in the VASPBERRY code[39–41].

#### IV. CRYSTAL AND ELECTRONIC STRUCTURES

It has been proved that  $\text{CrMoC}_2\text{S}_6$  monolayer possesses dynamical and thermal stabilities, and the experimental possibility is also confirmed by the formation energy[30]. Here, we also calculate two independent elastic constants:  $C_{11} = 91.69 \text{ Nm}^{-1}$  and  $C_{12} = 34.57 \text{ Nm}^{-1}$ , which satisfy the Born criteria of mechanical stability[42]:  $C_{11} > 0$  and  $C_{11} - C_{12} > 0$ , confirming its mechanical stability. The crystal structures of  $\text{CrMoC}_2\text{S}_6$  are shown in Figure 2 (a) and (b), which crystallizes in the  $P312$  space group (No.149), lacking spatial inversion symmetry. The  $\text{CrMoC}_2\text{S}_6$  can be obtained by substituting one Cr of  $\text{Cr}_2\text{C}_2\text{S}_6$  with Mo via isovalent alloying. The Cr

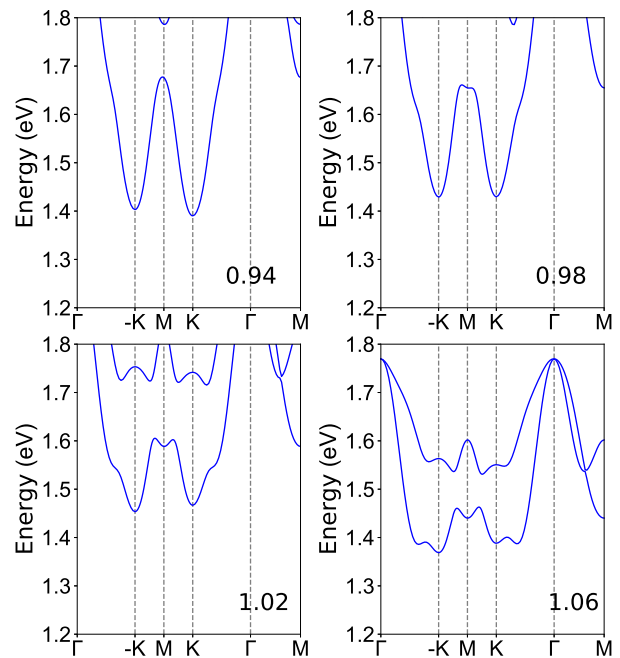


FIG. 4. (Color online) For  $\text{CrMoC}_2\text{S}_6$ , the energy band structures of conduction bands near the Fermi energy level with SOC at representative  $a/a_0$  (0.94, 0.98, 1.02, 1.06).

and Mo are surrounded by six S atoms, forming a honeycomb lattice. Two  $\text{CS}_3$  moieties are connected by two C atoms, forming a dumbbell-like structure. The optimized equilibrium lattice constants of  $\text{CrMoC}_2\text{S}_6$  are  $a=b=5.714 \text{ \AA}$  by GGA+ $U$  method. To determine magnetic ground state of  $\text{CrMoC}_2\text{S}_6$ , the FM and three AFM configurations (AFM1, AFM2 and AFM3) are constructed (FIG.S1 of electronic supplementary information (ESI)), and the AFM1 is called Néel AFM state. The energy of AFM1 per unit cell is 580 meV, 365 meV and 191 meV lower than those of FM, AFM2 and AFM3 cases, confirming that the  $\text{CrMoC}_2\text{S}_6$  possesses AFM1 ground state.

The energy band structures of  $\text{CrMoC}_2\text{S}_6$  and  $\text{Cr}_2\text{C}_2\text{S}_6$  without SOC are plotted in Figure 2 (c) and FIG.S2 of ESI, respectively. The lattice of  $\text{Cr}_2\text{C}_2\text{S}_6$  has spatial inversion symmetry, but the inversion symmetry will disappear with AFM1 ordering. However, a combination of inversion symmetry  $P$  and time-reversal symmetry  $T$  ( $PT$ ) exist, which leads to disappeared spin splitting. For  $\text{CrMoC}_2\text{S}_6$ , the large spin splitting around the Fermi energy level can be observed, and the total magnetic moment per unit cell is strictly  $0.00 \mu_B$ . It is clearly seen that  $\text{CrMoC}_2\text{S}_6$  is an indirect gap semiconductor with conduction band bottom (CBM)/valence band maximum (VBM) at K/ $\Gamma$  point, and the energies of -K and K valleys in the conduction bands are degenerate. Monolayer  $\text{CrMoC}_2\text{S}_6$  is a bipolar AFM semiconductor with VBM and CBM in different spin channels.

When including SOC, the magnetic orientation of  $\text{CrMoC}_2\text{S}_6$  should be determined by MAE, and

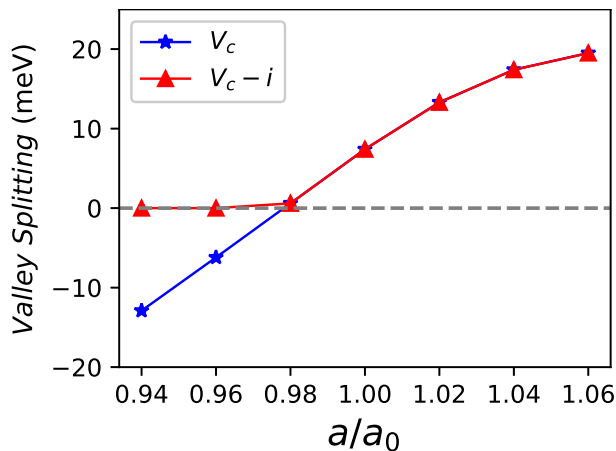


FIG. 5. (Color online) For  $\text{CrMoC}_2\text{S}_6$ , the valley splitting with assumed out-of-plane and intrinsic magnetization direction ( $V_c$  and  $V_c - i$ ) for conduction band as a function of  $a/a_0$ .

only out-of-plane case can produce spontaneous valley polarization[27]. The MAE can be calculated by  $E_{MAE} = E_{SOC}^{\parallel} - E_{SOC}^{\perp}$ , where  $\parallel$  and  $\perp$  mean that spins lie in the plane and out-of-plane. The positive MAE means out-of-plane magnetic anisotropy, while the negative value indicates in-plane one. The predicted MAE is  $148\mu\text{eV}/\text{unit cell}$ , which means the out-of-plane easy magnetization axis of  $\text{CrMoC}_2\text{S}_6$ . The energy band structures of  $\text{CrMoC}_2\text{S}_6$  with SOC are plotted in Figure 2 (d), which shows the valley polarization with the valley splitting of only 7.4 meV ( $\Delta E_C = E_K^C - E_{-K}^C$ ), and the energy of K valley is higher than one of -K valley. In order to strengthen valley splitting, strain engineering may be an effective and feasible method[43]. In the next section, we will study the strain effects on magnetic and electronic properties of  $\text{CrMoC}_2\text{S}_6$ .

## V. STRAIN EFFECTS

Here, the  $a/a_0$  (0.94~1.06) is used to simulate the biaxial strain, where  $a$  and  $a_0$  are the strained and unstrained lattice constants, respectively. The  $a/a_0 < 1 > 1$  means the compressive/tensile strain. Firstly, we determine the magnetic ground state of strained  $\text{CrMoC}_2\text{S}_6$  by the energy difference between FM/AFM2/AFM3 and AFM1 configurations, which is shown in Figure 3 (a). Within considered  $a/a_0$  range, the AFM1 ordering is always ground state. With increasing strain, the strength of the magnetic interaction is reduced. To maintain spontaneous valley polarization, the direction of magnetization is another key factor. The MAE vs  $a/a_0$  is plotted in Figure 3 (b), which shows a transition of magnetization direction. Compressive strain can make the magnetization direction of  $\text{CrMoC}_2\text{S}_6$  change from out-of-plane case to in-plane case, and this critical strain point is about 0.98. Fortunately, tensile strain can enhance the

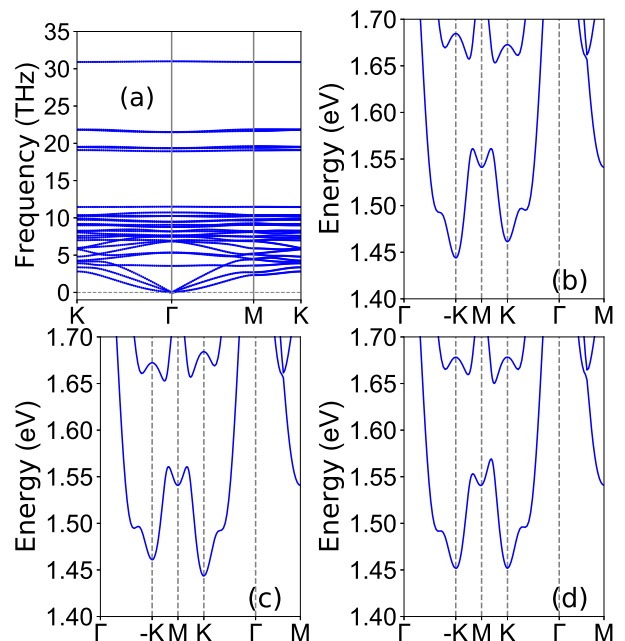


FIG. 6. (Color online) For  $\text{CrMoC}_2\text{S}_6$  with  $a/a_0=1.04$ , the phonon dispersion curves (a); the energy band structures of conduction bands near the Fermi energy level with SOC (b, c, d) for magnetization direction along the positive  $z$ , negative  $z$ , and positive  $x$  direction, respectively.

MAE of  $\text{CrMoC}_2\text{S}_6$ , thereby promoting the spontaneous valley polarization.

The energy band structures of  $\text{CrMoC}_2\text{S}_6$  at representative  $a/a_0$  by using both GGA and GGA+SOC are plotted in FIG.S3 of ESI, and the enlarged figures of SOC energy band structures near the Fermi energy level for the conduction band are plotted in Figure 4. The valley splitting with assumed out-of-plane and intrinsic magnetization direction for conduction band as a function of  $a/a_0$  are plotted in Figure 5. Based on FIG.S3 of ESI,  $\text{CrMoC}_2\text{S}_6$  is always a bipolar AFM semiconductor. Near the Fermi energy level, the conduction bands come from spin-up channel, while the valence band is dominated by spin-down channel. With assumed out-of-plane magnetization, the compressive strain can induce K valley polarization, while the tensile strain maintains -K valley polarization. Both increasing compressive and tensile strains can enhance the absolute size of valley splitting  $|\Delta E_C|$ . From this perspective, strain can be considered analogous to a pseudomagnetic field. Strain-driven valley polarization transition can also be observed in Janus  $\text{GdClF}$  monolayer[44]. When considering intrinsic magnetic anisotropy, the spontaneous valley polarization appears with  $a/a_0$  being larger than 0.98. At  $a/a_0=1.06$ , the corresponding valley splitting is about 19.5 meV.

Finally, taking a typical  $a/a_0=1.04$ , the physical properties of  $\text{CrMoC}_2\text{S}_6$  are detailedly investigated. The calculated phonon spectrum of  $\text{CrMoC}_2\text{S}_6$  with  $a/a_0=1.04$  is shown in Figure 6 (a), which shows no obvious imaginary frequencies, indicating its dynamic stability. The

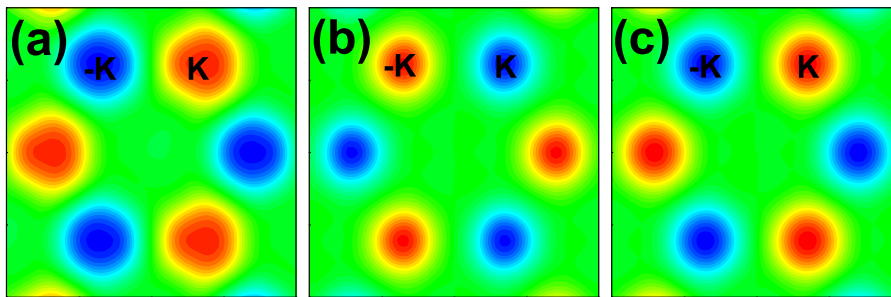


FIG. 7. (Color online) For  $\text{CrMoC}_2\text{S}_6$  with  $a/a_0=1.04$ , the distribution of Berry curvatures of total (a), spin-up (b) and spin-down (c).

TABLE I. For monolayer  $\text{CrMoC}_2\text{S}_6$  with  $a/a_0 = 1.04$  at different  $U$  values, the energies of FM, AFM1, AFM2 and AFM3 ordering (meV); the MAE/unit cell in  $\mu\text{eV}$ ; the valley splitting ( $V_c$ ) for conduction band (meV).

$U$ (Cr, Mo)	$E_{FM}$	$E_{AFM1}$	$E_{AFM2}$	$E_{AFM3}$	MAE	$V_c$
(3,2)	371	0	231	128	478	16.5
(3,3)	339	0	214	122	419	17.4
(4,3)	292	0	181	107	416	18.2

energy band structures of conduction bands near the Fermi energy level with SOC for magnetization direction along the positive  $z$ , negative  $z$ , and positive  $x$  directions are plotted in Figure 6 (b), (c) and (d). Figure 6 (b) shows the valley polarization with the valley splitting of 17.4 meV, and the energy of K valley is higher than one of -K valley. Figure 6 (c) indicates that the valley polarization can be switched by reversing the magnetization direction. When the magnetization direction of  $\text{CrMoC}_2\text{S}_6$  is in-plane (see Figure 6 (d)), no valley polarization can be observed.

For  $\text{CrMoC}_2\text{S}_6$  at  $a/a_0=1.04$ , the distribution of Berry curvatures of total, spin-up and spin-down are plotted in Figure 7. For purposes of comparison, the related distribution of Berry curvatures of  $\text{Cr}_2\text{C}_2\text{S}_6$  are also shown in FIG.S4 of ESI. Due to  $PT$  symmetry, the total Berry curvatures of  $\text{Cr}_2\text{C}_2\text{S}_6$  are zero, but the berry curvatures are opposite for the same valley at different spin channel and different valley at the same spin channel. However, for  $\text{CrMoC}_2\text{S}_6$ , the total Berry curvatures are nonzero at -K and K valley due to broken  $PT$  symmetry. The Berry curvatures of the -K and K valleys have opposite signs for the same spin channel, and the Berry curvatures are also opposite for the same valley at different spin channel. With an applied longitudinal in-plane electric field, the Bloch carriers will acquire an anomalous transverse velocity  $v_\perp \sim E_\parallel \times \Omega(k)$  [4]. When the Fermi energy level is shifted between the -K and K valleys in the conduction band, the spin-up carriers from -K valley will accumulate along one edge of the sample, resulting in the AVHE (Figure 1 (f)).

In general, 3d electrons have a stronger electron correlation than 4d electrons. For monolayer  $\text{CrMoC}_2\text{S}_6$  at

$a/a_0 = 1.04$ , the different  $U$  (Cr, Mo) values are also considered to confirm the reliability of our results. From  $U$  (3, 2) to  $U$  (3, 3) to  $U$  (4, 3), the magnetic interaction energy and MAE of  $\text{CrMoC}_2\text{S}_6$  become weak, but it always possesses out-of-plane AFM1 ordering. At different  $U$  (Cr, Mo) values, the energy band structures of conduction bands near the Fermi energy level with SOC for magnetization direction along the positive  $z$  direction are plotted in FIG.S5 of ESI. They all show -K valley polarization, and the valley splitting increases with increasing  $U$  (Cr, Mo). The related data are summarized in Table I.

To elucidate mechanical performance of  $\text{CrMoC}_2\text{S}_6$ , the isotropic in-plane Young's modulus  $C_{2D}$  of  $78.66 \text{ Nm}^{-1}$  is predicted. This is weaker than graphene ( $\sim 340 \pm 40 \text{ Nm}^{-1}$ ) and  $\text{MoS}_2$  ( $\sim 126.2 \text{ Nm}^{-1}$ ) [45, 46], indicating the better mechanical flexibility of monolayer  $\text{CrMoC}_2\text{S}_6$ , which is in favour of experimentally enhancing valley splitting by strain. For  $\text{MoS}_2$  monolayer, the strain with as large as 5.6% has been achieved experimentally [47]. Therefore, the 1.04 (4%) strain in  $\text{CrMoC}_2\text{S}_6$  can be realized experimentally due to small  $C_{2D}$ .

## VI. CONCLUSION

In summary, we present a way to induce AVHE in hexagonal AFM monolayer by isovalent alloying. By the first-principles calculations, we confirm the validity of our proposed way by an extensive study of  $\text{CrMoC}_2\text{S}_6$  monolayer. Due to broken  $P$  and  $T$  symmetries in  $\text{CrMoC}_2\text{S}_6$ , there is a spontaneous valley polarization. Moreover, the spin splitting can occur due to broken  $PT$  symmetry, which can also be explained by  $d$  orbital mismatch of different magnetic atoms. Strain engineering can be used to tune valley splitting, and calculated results show that tensile strain can enhance the valley splitting of  $\text{CrMoC}_2\text{S}_6$  with the out-of-plane AFM1 ordering. With an applied longitudinal in-plane electric field, the Berry curvature can produce AVHE. Our works are expected to speed up the realization of AVHE in AFM monolayers, and provide a route for constructing energy-efficient and ultrafast valleytronic devices.

## ACKNOWLEDGMENTS

This work is supported by Natural Science Basis Research Plan in Shaanxi Province of China (2021JM-456).

We are grateful to Shanxi Supercomputing Center of China, and the calculations were performed on TianHe-2.

- 
- [1] J. R. Schaibley, H. Yu, G. Clark, P. Rivera, J. S. Ross, K. L. Seyler, W. Yao and X. Xu, *Nat. Rev. Mater.* **1**, 16055 (2016).
- [2] G. Pacchioni, *Nat. Rev. Mater.* **5**, 480 (2020).
- [3] S. A. Vitale, D. Nezhich, J. O. Varghese, P. Kim, N. Gedik, P. Jarillo-Herrero, D. Xiao and M. Rothschild, *Small* **14**, 1801483 (2018).
- [4] D. Xiao, M. C. Chang and Q. Niu, *Rev. Mod. Phys.* **82**, 1959 (2010).
- [5] A. Srivastava, M. Sidler, A. V. Allain, D. S. Lembke, A. Kis and A. Imamoglu, *Nat. Phys.* **11**, 141 (2015).
- [6] K. F. Mak, K. He, J. Shan and T. F. Heinz, *Nat. Nanotechnol.* **7**, 494 (2012).
- [7] H. Zeng, J. Dai, W. Yao, D. Xiao, and X. Cui, *Nat. Nanotechnol.* **7**, 490 (2012).
- [8] M. Zeng, Y. Xiao, J. Liu, K. Yang and L. Fu, *Chem. Rev.* **118**, 6236 (2018).
- [9] C. Zhao, T. Norden, P. Zhang, P. Zhao, Y. Cheng, F. Sun, J. P. Parry, P. Taheri, J. Wang, Y. Yang, T. Scrace, K. Kang, S. Yang, G. Miao, R. Sabirianov, G. Kioseoglou, W. Huang, A. Petrou and H. Zeng, *Nat. Nanotechnol.* **12**, 757 (2017).
- [10] D. MacNeill, C. Heikes, K. F. Mak, Z. Anderson, A. Kormányos, V. Zólyomi, J. Park and D. C. Ralph, *Phys. Rev. Lett.* **114**, 037401 (2015).
- [11] X. X. Zhang, Y. Lai, E. Dohner, S. Moon, T. Taniguchi, K. Watanabe, D. Smirnov and T. F. Heinz, *Phys. Rev. Lett.* **122**, 127401 (2019).
- [12] T. Cao, G. Wang, W. Han, H. Ye, C. Zhu, J. Shi, Q. Niu, P. Tan, E. Wang, B. Liu and J. Feng, *Nat. Commun.* **3**, 887 (2012).
- [13] W. Y. Tong, S. J. Gong, X. Wan and C. G. Duan, *Nat. Commun.* **7**, 13612 (2016).
- [14] Y. B. Liu, T. Zhang, K. Y. Dou, W. H. Du, R. Peng, Y. Dai, B. B. Huang, and Y. D. Ma, *J. Phys. Chem. Lett.* **12**, 8341 (2021).
- [15] Z. Song, X. Sun, J. Zheng, F. Pan, Y. Hou, M.-H. Yung, J. Yang, and J. Lu, *Nanoscale* **10**, 13986 (2018).
- [16] J. Zhou, Y. P. Feng, and L. Shen, *Phys. Rev. B* **102**, 180407(R) (2020).
- [17] P. Zhao, Y. Ma, C. Lei, H. Wang, B. Huang, and Y. Dai, *Appl. Phys. Lett.* **115**, 261605 (2019).
- [18] X. Y. Feng, X. L. Xu, Z. L. He, R. Peng, Y. Dai, B. B. Huang and Y. D. Ma, *Phys. Rev. B* **104**, 075421 (2021).
- [19] Y. Zang, Y. Ma, R. Peng, H. Wang, B. Huang, and Y. Dai, *Nano Res.* **14**, 834 (2021).
- [20] R. Peng, Y. Ma, X. Xu, Z. He, B. Huang, and Y. Dai, *Phys. Rev. B* **102**, 035412 (2020).
- [21] W. Du, Y. Ma, R. Peng, H. Wang, B. Huang, and Y. Dai, *J. Mater. Chem. C* **8**, 13220 (2020).
- [22] R. Li, J. W. Jiang, W. B. Mi and H. L. Bai, *Nanoscale* **13**, 14807 (2021).
- [23] T. Jungwirth, J. Sinova, A. Manchon, X. Marti, J. Wunderlich, and C. Felser, *Nat. Phys.* **14**, 200 (2018).
- [24] T. Zhao, S. Xing, J. Zhou, N. Miao and Z. Sun, *Journal of Materiomics* **10**, 269 (2024).
- [25] W. Du, R. Peng, Z. He, Y. Dai, B. Huang, and Y. Ma, *npj 2D Mater. Appl.* **6**, 11 (2022).
- [26] Y. Xu, H. Liu, Y. Dai, B. Huang and W. Wei, *Appl. Phys. Lett.* **122**, 242404 (2023).
- [27] S. D. Guo, Y. L. Tao, Z. Y. Zhuo, G. Zhu and Y. S. Ang, *Phys. Rev. B* **109**, 134402 (2024).
- [28] S. D. Guo, W. Xu, Y. Xue, G. Zhu and Y. S. Ang, *Phys. Rev. B* **109**, 134426 (2024).
- [29] X. Li, X. Wu, Z. Li and J. Yang, *Phys. Rev. B* **92**, 125202 (2015).
- [30] P. Wang, D. X. Wu, K. Zhang and X. J. Wu, *J. Phys. Chem. Lett.* **13**, 3850 (2022).
- [31] P. Hohenberg and W. Kohn, *Phys. Rev.* **136**, B864 (1964); W. Kohn and L. J. Sham, *Phys. Rev.* **140**, A1133 (1965).
- [32] G. Kresse, *J. Non-Cryst. Solids* **193**, 222 (1995).
- [33] G. Kresse and J. Furthmüller, *Comput. Mater. Sci.* **6**, **15** (1996).
- [34] G. Kresse and D. Joubert, *Phys. Rev. B* **59**, 1758 (1999).
- [35] J. P. Perdew, K. Burke and M. Ernzerhof, *Phys. Rev. Lett.* **77**, 3865 (1996).
- [36] S. L. Dudarev, G. A. Botton, S. Y. Savrasov, C. J. Humphreys, and A. P. Sutton, *Phys. Rev. B* **57**, 1505 (1998).
- [37] A. Togo, F. Oba and I. Tanaka, *Phys. Rev. B* **78**, 134106 (2008).
- [38] T. Fukui, Y. Hatsugai and H. Suzuki, *J. Phys. Soc. Japan.* **74**, 1674 (2005).
- [39] H. J. Kim, <https://github.com/Infant83/VASPBERRY>, (2018).
- [40] H. J. Kim, C. Li, J. Feng, J.-H. Cho, and Z. Zhang, *Phys. Rev. B* **93**, 041404(R) (2016).
- [41] S. W. Kim, H. J. Kim, S. Cheon and T. H. Kim, *Phys. Rev. Lett.* **128**, 046401 (2022).
- [42] R. C. Andrew, R. E. Mapasha, A. M. Ukpong and N. Chetty, *Phys. Rev. B* **85**, 125428 (2012).
- [43] H. X. Cheng, J. Zhou, W. Ji, Y. N. Zhang and Y. P. Feng, *Phys. Rev. B* **103**, 125121 (2021).
- [44] S. D. Guo, X. S. Guo, X. X. Cai and B. G. Liu, *Phys. Chem. Chem. Phys.* **24**, 715 (2022).
- [45] K. N. Duerloo, M. T. Ong and E. J. Reed, *J. Phys. Chem. Lett.* **3**, 2871 (2012).
- [46] C. Lee, X. g Wei, J. W. Kysar and J. Hone, *Science* **321**, 385 (2008).
- [47] D. Lloyd, X. H. Liu, J. W. Christopher et al., *Nano Lett.* **16**, 5836 (2016).